

Atomic-scale magnetic modeling of oxide nanoparticles

R. H. Kodama* and A. E. Berkowitz

Physics Department & Center for Magnetic Recording Research, University of California, San Diego, La Jolla, California 92093

(Received 6 May 1998; revised manuscript received 13 October 1998)

We present a method for atomic-scale modeling of the magnetic behavior of ionic magnetic solids. Spin distributions and net magnetic moments are calculated for nanoparticles of ferrimagnetic NiFe_2O_4 and $\gamma\text{-Fe}_2\text{O}_3$, and antiferromagnetic NiO as a function of applied field. Calculations incorporate crystal structures and exchange parameters determined from bulk data, bulk anisotropy for core spins, reasonable estimates for the anisotropy of surface spins, and finite temperatures simulated by random perturbations of spins. Surface spin disorder was found in the case of ferrimagnetic spinel nanoparticles, due to broken exchange bonds at the surface. The calculations also demonstrate that surface anisotropy enhances the coercivity of such particles only when surface spin disorder is present. Simulated thermal perturbations were used to characterize the distribution of energy barriers between surface spin states of such particles. The distribution of barriers can explain the macroscopic quantum tunneling like magnetic relaxation at low temperatures found experimentally. Calculations on NiO nanoparticles predict eight, six, or four-sublattice spin configurations in contrast to the two-sublattice configuration accepted for bulk NiO . Relatively weak coupling between the multiple sublattices allows a variety of reversal paths for the spins upon cycling the applied field, resulting in large coercivities and loop shifts, in qualitative agreement with experiment. [S0163-1829(99)00509-3]

I. INTRODUCTION

Finite-size effects dominate the magnetic properties of nanosized particles, and become more important as the particle size decreases. In many cases, they arise because of the competition between surface magnetic properties and core magnetic properties. These effects are of intense technological interest because of their relevance to the stability of information stored in the form of magnetized particles, which compose rigid disk, floppy disk, and tape recording media. This industry is driving towards higher densities of stored “bits,” which necessitates the use of smaller particles in the media, making a basic understanding of finite-size effects critical. More generally, surface and interface effects such as the spin disorder which we find in nanoparticles have relevance to thin-film devices in the new breed of magnetoelectronics, e.g., spin valves, spin transistors, spin-dependent tunneling devices. Since spin transport through magnetic/nonmagnetic interfaces plays an important role in these devices, the state of interfacial magnetic moments will impact device performance.

The most obvious and heavily studied finite-size effect is superparamagnetism. The basic principle is that the magnetic anisotropy energy, which keeps a particle magnetized in a particular direction, is generally proportional to the particle volume. Therefore, at a certain temperature there is a critical size below which thermal excitations are sufficient to rotate the particle magnetization, thus demagnetizing an assembly of such particles. Although this is a well-studied effect, it is understood only on a phenomenological level. The mechanism by which external thermal excitations such as phonons couple to the particle magnetization, the trajectory by which the individual atomic moments reverse (i.e., “reversal mode”), and the influence of microstructural details are some of the unknowns.

A more fundamental question is how the “ground state”

of a magnetic nanoparticle is influenced by the finite size. One of the principal results of this work is that the magnetic ground state of nanoparticles can be severely altered with respect to the conventional assumption that they are single magnetic domains, having the same basic spin configuration found in bulk materials. We find that the ground state is strongly influenced by microstructural details of the surface, and we demonstrate the connection between new ground state and thermally activated relaxation of the magnetic moment.

Our previous publications have focused on the experimental evidence for finite-size effects in NiFe_2O_4 (Refs. 1 and 2) and NiO (Ref. 3) nanoparticles as well as salient modeling results. The intent of this paper is to describe the modeling methodology in detail, and present its application to NiFe_2O_4 , $\gamma\text{-Fe}_2\text{O}_3$, and NiO as examples. Special emphasis will be given to results on the influence of surface anisotropy in NiFe_2O_4 and $\gamma\text{-Fe}_2\text{O}_3$.

Magnetic relaxation. To set the context for our discussion of thermally activated and quantum tunneling magnetization reversal, we will briefly review the relevant theories. The magnetic anisotropy energy of a particle due to bulk magnetocrystalline and shape anisotropy is proportional to the particle volume. Therefore, we can express the energy barrier that has to be overcome to reverse the particle magnetization as $E = KV$, where K is an effective anisotropy constant. Using the formalism of thermal activation, we can express the frequency of thermally activated reversals as

$$f = f_0 e^{-E/k_B T},$$

where f_0 is the “attempt frequency” which has been estimated for various materials to be in the range from 10^9 to 10^{13} s^{-1} . If the magnetization of a collection of particles is measured in a regime where the observation time is compa-

rable to f^{-1} , then the moment will relax during the measurement, a phenomenon known as magnetic viscosity. Following the analysis by Street and Woolley⁴ and more recently by Barbara *et al.*,⁵ the magnetization as a function of time after changing the applied field is the following:

$$M(t) = M_0 \left(1 - \int_0^{E_c} e^{-t f} n(E) dE \right), \quad (1)$$

where $n(E)dE$ is the fraction of particles having an energy barrier between E and $E + dE$. The exponential factor in Eq. (1) has an abrupt step as a function of E , near $k_B T \ln(tf_0)$. The narrow energy range spanned by this step can be described as the ‘‘experimental window’’ of the measurement. Assuming $n(E)$ is a smooth function relative to changes in the exponential factor, it has been shown⁵ that

$$M(t) = M_0 (1 - n(\bar{E}) k_B T \ln(tf_0)),$$

where \bar{E} is the mean energy barrier within the experimental window, and we identify the viscosity parameter

$$S = - \frac{1}{M_0} \frac{dM}{d(\ln t)} = n(\bar{E}) k_B T.$$

The experimental window sweeps over different parts of $n(E)$ as the temperature is changed. For example, if the barrier distribution is constant over a range of energies, then the viscosity parameter will be linear in T over the corresponding temperature range. If instead the barrier distribution turns up at lower energies, the viscosity parameter may level off or increase as the temperature is lowered. Specifically, if the barrier distribution has the form $n(E) = 1/E$ at low energies, then the viscosity will become temperature independent at low temperatures. This type of barrier distribution is *not* consistent with $E = KV$, but as we will discuss in Sec. III, could arise from spin-glass-like surface states of a particle.

The mechanism of quantum tunneling for spontaneous magnetization reversal of small particles was suggested some time ago by Bean and Livingston,⁶ and more recently developed theoretically by a number of authors.⁷⁻⁹ Macroscopic quantum tunneling (MQT), or more specifically quantum tunneling of magnetization, is essentially quantum-mechanical nonconservation of the ‘‘z’’ component of a macroscopic spin (single domain particle) due to off-diagonal terms in the spin Hamiltonian. Chudnovsky and Gunther⁷ predicted for the case of orthorhombic symmetry, a crossover temperature into the quantum tunneling regime

$$T^* = \frac{3\hbar \gamma \sqrt{K_1 K_2 \varepsilon}}{8k_B M_0}.$$

We expect a high crossover temperature (few K) for particles having high anisotropy, and a crossover temperature lower than typical measurement capability (few mK) for particles having low anisotropy. If we approximate the temperature dependence of the viscosity parameter as being linear in T for the thermally activated regime, the full prediction of the MQT model is that the viscosity parameter is linear in T at high temperatures, becoming independent of temperature below T^* . In Sec. III we investigate the zero-field relaxation of NiFe₂O₄ nanoparticles. As an example, we calculate the

crossover temperature for particles having the same cubic anisotropy as bulk NiFe₂O₄. In the above formula, we set $K_1 = K_2 = K_1$ (cubic, bulk NiFe₂O₄) = 8×10^4 ergs/cc, and set $M_0 = 300$ emu/cc, resulting in $T^* = 13$ mK at zero field. What we observe experimentally, is an apparent crossover temperature of 2 K, which is 150 times larger. One could argue that the effective anisotropy of these particles is enhanced by surface anisotropy, but as we will show, surface anisotropy tends to average to zero for a well-ordered, single-domain particle. We find that in order for the surface anisotropy to have an effect, it is necessary to have spin disorder on the surface. Therefore, it is difficult to reconcile these experimental and theoretical observations with a quantum tunneling model which assumes particles to be well-ordered single domains. Rather, we prefer a description in terms of thermal activation of a barrier distribution like $1/E$ at low energies which we are able to calculate for spin-glass-like surface states of NiFe₂O₄ nanoparticles.

II. ATOMIC-SCALE MAGNETIC MODELING

A. Background

Finite-element modeling of magnetic materials, commonly known as ‘‘micromagnetic modeling,’’¹⁰ has been used extensively in recent years. It has been applied to study problems such as transition noise in magnetic recording media,¹¹ reversal modes of magnetic particles,^{12,13} and domain structure in soft magnetic films.^{14,15} Typically, the magnetic body is subdivided into several hundred or thousand volume elements which are considered to have uniform magnetization. Exchange, anisotropy, magnetostatic, and Zeeman energies are calculated based on the orientation of the magnetization of each element. The total energy is then minimized by some algorithm to obtain the magnetization distribution. Such techniques are particularly suited to the study of macroscopic systems, with dimensions on the order of microns, since the surface-to-volume ratio is relatively small, making a detailed consideration of surface microstructure and surface magnetism less important in determining the overall behavior. Practically, it is beyond current computing power to treat each atomic moment individually for systems of this size, since a cubic micron contains approximately 10^{11} atoms.

In the present work, we consider magnetic behavior of particles having diameters from 1–7 nm. On this scale, surface atoms make up at least 25% of the total number of atoms in a particle. The high surface-to-volume ratio makes a detailed consideration of surface microstructure and the behavior of individual atomic moments critical in understanding the overall behavior. Since the total number of magnetic atoms is less than 10^4 for these sizes, it also becomes practical to treat atoms individually in calculations of magnetization distributions. This section will present the basic approach of these calculations, with more detail on specific systems described in later sections. Other examples of such atomic scale magnetic modeling in the literature are work by Koon and co-workers^{16,17} on interlayer exchange coupling and random anisotropy systems, and by Pappas *et al.*¹⁸ on spin configurations in Gd clusters.

B. Bulk and surface parameters

The first step in each calculation is a survey of the experimental and theoretical literature on the bulk magnetic properties of the material in question. Exchange constants are typically found by fitting moment vs temperature data to a mean-field theory or fitting inelastic neutron scattering data to a spin Hamiltonian. Anisotropy constants are found by torque magnetometry or inelastic neutron scattering. We assume for the calculations that the pairwise exchange interactions have the same magnitude for bulk and surface atoms, but that the total exchange interaction is less for surface atoms because of their lower coordination (i.e., fewer neighbors). As discussed above, we postulate the existence of ‘‘broken exchange bonds’’ due to oxygen vacancies or bonding with ligands other than oxygen at the surface. In short, we set the exchange constant for pairs of atoms equal to the bulk value, or equal to zero for some fraction of pairs of spins at the surface. This fraction of broken exchange bonds between surface atoms we term the broken bond density (BBD).

The magnetocrystalline anisotropy reflects the symmetry of the neighbors of each atom, so it is reasonable to use bulk anisotropy for atoms in the core of the particle. We simply take the bulk anisotropy values in ergs/cm³ and divide by the number of atoms per cm³ and apply it as a single-ion anisotropy to all the atoms in the core. However, the large perturbations to the crystal symmetry at surfaces, should lead to magnetocrystalline anisotropy of different magnitude and symmetry for surface sites. Néel proposed this phenomenon of surface anisotropy in 1954.¹⁹ For the purpose of our calculations, we do not make a detailed theory of the anisotropy at each particular surface site. Rather, we can say that the symmetry of a surface site is uniaxial to lowest order, hence

$$E_A = -k_S \cos^2 \theta \quad (2)$$

(lower case ‘‘k’’ is used because it is in units of energy per cation, rather than energy per unit volume denoted by upper case ‘‘K’’) and we assume that we have an *easy-axis* anisotropy, i.e., $k_S > 0$, rather than an *easy-plane* anisotropy. We define the easy axis $\hat{\mathbf{u}}$ as the dipole moment of the nearest-neighbor (oxygen ion) positions relative to a surface atom as follows:

$$\hat{\mathbf{u}}_i \propto \sum_j^{\text{nn}} (\mathbf{P}_j - \mathbf{P}_i), \quad (3)$$

where \mathbf{P}_i is the position of the i th atom and the sum is over the nearest neighbors of the i th atom. Since some of the neighbors are missing for a surface atom, $\hat{\mathbf{u}}_i$ will be nonzero and directed approximately normal to the surface. The magnitude of the surface anisotropy has not been determined experimentally in magnetic oxides. Nevertheless, some indication of the magnitude of surface anisotropies can be obtained by examining the literature on EPR measurements of dilute magnetic ions in bulk crystals of nonmagnetic oxides.^{20,21} It is found that when the magnetic ions are substituted into sites having low symmetry, rather large anisotropies are obtained, even for ions such as Ni²⁺ and Fe³⁺ which have singlet ground states (i.e., low anisotropy) in cubic sites.²² Values of k_S between 1 and 4 k_B /cation were

used in the calculations, and are representative of the magnitudes found by EPR. The total spin Hamiltonian is then

$$\begin{aligned} \mathcal{H} = & \sum_i^{\{\text{all spins}\}} -g_i \mu_B S_i \hat{\mathbf{S}}_i \cdot \left[\mathbf{H} + \frac{1}{2} \mathbf{H}_{\text{int},i} \right] + E_{A,i}, \\ E_{A,i} = & \begin{cases} E_{A,\text{bulk}}(\hat{\mathbf{S}}_i), & \text{core cations} \\ -k_S (\hat{\mathbf{S}}_i \cdot \hat{\mathbf{u}}_i)^2, & \text{surface cations,} \end{cases} \\ \mathbf{H}_{\text{int}} = & \sum_j^{\{\text{nn}\}} \frac{2J_{ij} S_j}{g_i \mu_B} \hat{\mathbf{S}}_i + \sum_{j \neq i}^{\{\text{all spins}\}} g_j \mu_B S_j \frac{3\hat{\mathbf{r}}_{ji}(\hat{\mathbf{r}}_{ji} \cdot \hat{\mathbf{S}}_j) - \hat{\mathbf{S}}_j}{|\mathbf{r}_{ji}|^3}, \end{aligned} \quad (4)$$

where $g_i \mu_B S_i$ is the magnitude of the ionic moment and the unit vector $\hat{\mathbf{S}}_i$ gives its direction. The summation over {nn} denotes first- and second-nearest neighbors. The dipolar terms are included here for completeness, but they are neglected for the nanoparticle calculations since the intraparticle dipolar interactions are included in experimental determinations of bulk magnetocrystalline anisotropy, and shape anisotropy will be small since we only consider nearly spherical particles or antiferromagnets which have very small net magnetization.

C. Construction of a nanoparticle

The model nanoparticle is generated by putting magnetic ions on lattice sites corresponding to the bulk crystal structure. The particle surface is initially defined as either an ellipsoid or platelet of fixed elliptical cross section, and lattice sites within this volume are occupied with the appropriate ions. A variety of distinct particles of the same shape can be obtained by varying the center position of the ellipsoid or platelet within the crystal unit cell. Exchange bonds are set up between neighbors using the bulk exchange constants obtained from the literature. Typically, this includes first- and second-nearest neighbors, and different exchange constants between different ion species in the case of the ferrites. We refer to as ‘‘surface cations’’ those with lower than bulk coordination. Surface roughness is created by removing surface cations at random. The fraction of surface cations removed in this way we refer to as the surface vacancy density (SVD). After this procedure we remove any asperities, which we define as cations with fewer than two nearest cation neighbors. As indicated above, a fraction of exchange interactions between surface cations are removed from the first summation in Eq. (4), effectively breaking the exchange bond between them.

D. Energy minimization

Energy minimization algorithms in common use for micromagnetic modeling arise from the Landau-Lifshitz-Gilbert equation¹⁰

$$\frac{d\mathbf{m}}{dt} = \gamma_0 \mathbf{m} \times \mathbf{H}_{\text{eff}} - \lambda \mathbf{m} \times (\mathbf{m} \times \mathbf{H}_{\text{eff}}), \quad (5)$$

where γ_0 is the gyromagnetic ratio and λ is the damping constant. The first term on the right-hand side corresponds to precession about \mathbf{H}_{eff} and the second term corresponds to a

damping that brings the moment vector closer to \mathbf{H}_{eff} . For low-frequency problems, the precession term is typically discarded. A common approach is to iteratively update the orientation of the magnetization \mathbf{m} of each element based on the value of \mathbf{H}_{eff} determined by the orientation of all the other elements. Usually, \mathbf{m} is set parallel to the current direction of \mathbf{H}_{eff} , or rotated by some angle towards \mathbf{H}_{eff} . In some cases \mathbf{m} is rotated past the parallel orientation, a technique called ‘‘over-relaxation’’ which in some situations can lead to faster convergence.¹⁵ In the early stages of this work, such techniques were employed to do calculations of hysteresis loops of these nanoparticles. However, it was found that unreasonably high coercivities were obtained, and the coercivity was sensitive to the value of the relaxation parameter (the parameter which determines whether the moments are over-relaxed or under-relaxed). Furthermore, convergence was extremely slow, taking tens of thousands of iterations to reverse a particle containing 300 spins. We suspect that the relatively poor performance of this type of algorithm has to do with the large magnitude of exchange fields compared to applied fields (the effective exchange fields are greatly reduced when a system is discretized into elements containing many thousands of atoms as in micromagnetic models), as well as the exchange frustration and spin disorder which occurs at the surface of these nanoparticles.

Brown noted²³ in 1962 that the concept of a ‘‘local field’’ such as \mathbf{H}_{eff} is unreliable when the reversal of a magnetic system nucleates by a collective mode. Hence, for this and the previously stated reasons, we adopted an algorithm that goes beyond the ‘‘local field’’ and accounts for collective modes. The algorithm is a three-dimensional generalization

of one developed by Hughes²⁴ in 1983. Key points in this generalization were the choice of an appropriate coordinate system and the evaluation of energy derivatives. In our coordinate system, the spin unit vector was defined as a function of (α_i, β_i) which correspond to rotations in two orthogonal directions:

$$\hat{\mathbf{S}}_i(\alpha_i, \beta_i) = \frac{\hat{\mathbf{S}}_{0i} + \alpha_i \hat{\mathbf{e}}_{\alpha i} + \beta_i \hat{\mathbf{e}}_{\beta i}}{\sqrt{1 + \alpha_i^2 + \beta_i^2}}, \quad (6)$$

where $\hat{\mathbf{S}}_{0i}$ is the initial spin direction and $\hat{\mathbf{e}}_{\alpha i}$ and $\hat{\mathbf{e}}_{\beta i}$ are chosen to make $(\hat{\mathbf{e}}_{\alpha i}, \hat{\mathbf{e}}_{\beta i}, \hat{\mathbf{S}}_{0i})$ a mutually orthogonal set. It is easy to show that the rotation angle corresponding to a non-zero α or β is $\arctan \alpha$ or $\arctan \beta$, respectively, so for small rotation angles we can think of α and β being the rotation angles in radians. This choice of coordinates gives the following expressions for the derivatives of E (evaluated at $\alpha_i = \beta_i = 0$):

$$\begin{aligned} \frac{\partial E}{\partial \alpha_i} &= -g_i \mu_B S_i \hat{\mathbf{e}}_{\alpha i} \cdot \mathbf{H}_{\text{eff}}, \\ \mathbf{H}_{\text{eff}} &= \mathbf{H} + \mathbf{H}_{A,i} + \sum_j^{\{\text{nn}\}} \frac{2J_{ij} S_j}{g_i \mu_B} \hat{\mathbf{S}}_j \\ &+ \sum_{j \neq i}^{\{\text{all spins}\}} g_j \mu_B S_j \frac{3\hat{\mathbf{r}}_{ji}(\hat{\mathbf{r}}_{ji} \cdot \hat{\mathbf{S}}_j) - \hat{\mathbf{S}}_j}{|\mathbf{r}_{ji}|^3}. \end{aligned} \quad (7)$$

For uniaxial anisotropy (e.g., surface cations),

$$E_A = -k_u (\hat{\mathbf{S}}_i \cdot \hat{\mathbf{u}}_i)^2,$$

$$\mathbf{H}_{A,i} = \frac{2k_u (\hat{\mathbf{S}}_i \cdot \hat{\mathbf{u}}_i)}{g_i \mu_B S_i} \hat{\mathbf{u}}_i,$$

$$\frac{\partial^2 E}{\partial \alpha_j \partial \alpha_i} = \begin{cases} +g_i \mu_B S_i (\hat{\mathbf{S}}_{0i} \cdot \mathbf{H}_{\text{eff}}) - 2k_u (\hat{\mathbf{e}}_{\alpha i} \cdot \hat{\mathbf{u}}_i)^2, & i=j \\ -2J_{ij} S_i S_j \hat{\mathbf{e}}_{\alpha i} \cdot \hat{\mathbf{e}}_{\alpha j} - g_i g_j \mu_B^2 S_i S_j \left[\frac{3\hat{\mathbf{r}}_{ji}(\hat{\mathbf{r}}_{ji} \cdot \hat{\mathbf{e}}_{\alpha j}) - \hat{\mathbf{e}}_{\alpha j}}{|\mathbf{r}_{ji}|^3} \right] \cdot \hat{\mathbf{e}}_{\alpha i}, & i \neq j. \end{cases} \quad (8)$$

For cubic anisotropy,²⁵

$$E_A = k_1 (\hat{\mathbf{S}}_{ix}^2 \hat{\mathbf{S}}_{iy}^2 + \hat{\mathbf{S}}_{iy}^2 \hat{\mathbf{S}}_{iz}^2 + \hat{\mathbf{S}}_{iz}^2 \hat{\mathbf{S}}_{ix}^2),$$

$$\mathbf{H}_{A,i} = \frac{2k_1}{g_i \mu_B S_i} [\hat{\mathbf{S}}_{0ix} (\hat{\mathbf{S}}_{0iy}^2 + \hat{\mathbf{S}}_{0iz}^2), \hat{\mathbf{S}}_{0iy} (\hat{\mathbf{S}}_{0ix}^2 + \hat{\mathbf{S}}_{0iz}^2), \hat{\mathbf{S}}_{0iz} (\hat{\mathbf{S}}_{0ix}^2 + \hat{\mathbf{S}}_{0iy}^2)],$$

$$\frac{\partial^2 E}{\partial \alpha_j \partial \alpha_i} = \begin{cases} +g_i \mu_B S_i (\hat{\mathbf{S}}_{0i} \cdot \mathbf{H}_{\text{eff}}) - 2k_1 [1 - \hat{\mathbf{e}}_{\alpha ix}^2 \hat{\mathbf{S}}_{0ix}^2 - \hat{\mathbf{e}}_{\alpha iy}^2 \hat{\mathbf{S}}_{0iy}^2 - 5\hat{\mathbf{e}}_{\alpha iz}^2 \hat{\mathbf{S}}_{0iz}^2 + 4\hat{\mathbf{e}}_{\alpha ix} \hat{\mathbf{S}}_{0ix} \hat{\mathbf{e}}_{\alpha iy} \hat{\mathbf{S}}_{0iy}], & i=j \\ -2J_{ij} S_i S_j \hat{\mathbf{e}}_{\alpha i} \cdot \hat{\mathbf{e}}_{\alpha j} - g_i g_j \mu_B^2 S_i S_j \left[\frac{3\hat{\mathbf{r}}_{ji}(\hat{\mathbf{r}}_{ji} \cdot \hat{\mathbf{e}}_{\alpha j}) - \hat{\mathbf{e}}_{\alpha j}}{|\mathbf{r}_{ji}|^3} \right] \cdot \hat{\mathbf{e}}_{\alpha i}, & i \neq j. \end{cases} \quad (9)$$

Finally, for rhombohedral/hexagonal anisotropy (e.g., NiO), we have a uniaxial term plus the following:

the iteration, we found it more satisfactory, when $\vec{\mathbf{Q}} \cdot d\boldsymbol{\theta} < 0$, to allow the step in the unstable direction, since it represents a particularly good direction for reducing the energy, and simply terminate the iteration at that stage. In case the iteration produces a $d\boldsymbol{\theta}$ with very large rotation angles, we limit the maximum rotation to 0.1 radians in a final renormalization step. The conjugate directions algorithm is summarized below:

Initialization:

Calculate \mathbf{T} and $\vec{\mathbf{Q}}$,

$$d\boldsymbol{\theta}_0 = \mathbf{0}, \quad \mathbf{P}_0 = +\mathbf{T}, \quad \mathbf{R}_0 = -\mathbf{T}.$$

Repeat the following:

$$\lambda_m = \frac{-\mathbf{R}_m \cdot \mathbf{P}_m}{\mathbf{P}_m \cdot \vec{\mathbf{Q}} \cdot \mathbf{P}_m},$$

$$d\boldsymbol{\theta}_{m+1} = d\boldsymbol{\theta}_m + |\lambda_m| \mathbf{P}_m,$$

stop if $\lambda_m < 0$,

$$\mathbf{R}_{m+1} = \mathbf{R}_m + \lambda_m \vec{\mathbf{Q}} \cdot \mathbf{P}_m,$$

$$\varepsilon_m = \frac{\mathbf{R}_{m+1} \cdot \vec{\mathbf{Q}} \cdot \mathbf{P}_m}{\mathbf{P}_m \cdot \vec{\mathbf{Q}} \cdot \mathbf{P}_m},$$

$$\mathbf{P}_{m+1} = -\mathbf{R}_{m+1} + \varepsilon_m \mathbf{P}_m,$$

$$\delta E_{m+1} = \mathbf{T} \cdot d\boldsymbol{\theta}_{m+1} + \frac{1}{2} d\boldsymbol{\theta}_{m+1} \cdot \vec{\mathbf{Q}} \cdot d\boldsymbol{\theta}_{m+1},$$

stop if $|\delta E_{m+1}| < 1.2 |\delta E_m|$ and $\delta E_{m+1}, \delta E_m < 0$.

Renormalize $d\boldsymbol{\theta}$ (only if $\max d\boldsymbol{\theta} > 0.1$):

$$d\boldsymbol{\theta} = d\boldsymbol{\theta} \times (0.1 / \max d\boldsymbol{\theta}),$$

where $\max d\boldsymbol{\theta}$ is the largest component of $d\boldsymbol{\theta}$.

The algorithm is ‘‘smart’’ in the sense that when the system is far from equilibrium, it converges in 1–2 iterations and the resultant step is roughly in the direction of the local torques, whereas when the system is closer to equilibrium it may take 5–15 iterations, but the resultant step typically gives a factor of ten larger energy reduction than a step in the local torque direction. For zero-temperature calculations, it can be useful to treat situations where the torque vector is identically zero, such as when the system is at a saddle point in energy space. In this case, we initialize the auxiliary vectors $\mathbf{R}_m, \mathbf{P}_m$ with a random vector in place of \mathbf{T} , and proceed as usual.

The result of the conjugate directions algorithm represents a single step in the energy minimization procedure, which is summarized as follows:

Initialization:

(1) Compute total energy.

Repeat the following:

(2) Compute unit vectors $\hat{\mathbf{e}}_{\alpha i}, \hat{\mathbf{e}}_{\beta i}$,

(3) Compute effective fields,

(4) Stop if $\hat{\mathbf{e}}_{\alpha i} \cdot \hat{\mathbf{H}}_{\text{eff}}$ and $\hat{\mathbf{e}}_{\beta i} \cdot \hat{\mathbf{H}}_{\text{eff}} < 10^{-4}$ (i.e., $\hat{\mathbf{S}}_i$ parallel to \mathbf{H}_{eff} within 10^{-4} radians),

(5) Compute conjugate directions step,

(6) Update spin orientations,

(7) Compute total energy,

(8) If actual energy change is positive, shrink step length (e.g., $d\boldsymbol{\theta} = 0.6 \cdot d\boldsymbol{\theta}$) and repeat steps (6)–(8).

E. Finite temperature

Finite temperature is simulated by applying rotations to the spins in random directions between energy minimizations. The magnitude of rotations are adjusted to give a total-energy change $\Delta E = Nk_B T$, where N is the total number of spins. This is in contrast to the theory of superparamagnetism where each magnetic particle is given $k_B T$ of energy. In that case, the intraparticle degrees of freedom are assumed to be ‘‘frozen-out,’’ so that the particle behaves like a giant spin having only two rotational degrees of freedom. Since our model includes the intraparticle degrees of freedom, we must give $\frac{1}{2} k_B T$ of energy to each of the $2N$ rotational degrees of freedom. As the success of the superparamagnetic theory suggests, the ‘‘uniform mode’’ corresponding to uniform rotation of the particle moment is particularly important in describing the behavior. If we apply random rotations to each spin individually, the overlap of these rotations with the uniform mode approaches zero as N becomes large. Therefore, a better approach is to apply rotations to each spin resulting in $\Delta E = (N-1)k_B T$ plus a uniform rotation resulting in $\Delta E = k_B T$.

The details of the perturbation procedure are the following. First, we apply the uniform mode rotation as follows:

$$\hat{\mathbf{S}}_i^{\text{rot}} = \vec{\mathbf{R}}(\hat{\mathbf{n}}_R, \theta) \cdot \hat{\mathbf{S}}_{0i}, \quad (12)$$

where $\hat{\mathbf{n}}_R$ is a random unit vector, and $\vec{\mathbf{R}}(\hat{\mathbf{n}}_R, \theta)$ is the rotation matrix that rotates a three-vector about the axis $\hat{\mathbf{n}}_R$ by the angle θ .²⁶ The total energy is then calculated for the set of spin orientations, and the angle θ is optimized with a few steps of a linear search routine to give $\Delta E \approx k_B T$. Next, a similar procedure is applied to each spin. Here, a different method is used to rotate the spin in order to avoid calculating many trigonometric functions

$$\hat{\mathbf{S}}_i^{\text{rot}}(\alpha) = \frac{(1-|1-\alpha|)\hat{\mathbf{e}}_{\alpha i} + (1-\alpha)\hat{\mathbf{S}}_{0i}}{\sqrt{(1-|1-\alpha|)^2 + (1-\alpha)^2}}, \quad \hat{\mathbf{e}}_{\alpha i} = \frac{\hat{\mathbf{n}}_R \times \hat{\mathbf{S}}_{0i}}{\|\hat{\mathbf{n}}_R \times \hat{\mathbf{S}}_{0i}\|}. \quad (13)$$

We define an approximate expression for the energy change with respect to rotation of the i th spin:

$$\Delta E_{\text{local},i}(\alpha) \equiv g_i \mu_B S_i [\hat{\mathbf{S}}_{0i} - \hat{\mathbf{S}}_i^{\text{rot}}(\alpha)] \cdot \mathbf{H}_{\text{eff}}. \quad (14)$$

As we did for the uniform mode rotation, we optimize α with a linear search routine to give $\Delta E \approx k_B T$. The expression for $\Delta E_{\text{local},i}$ is exact if only the i th spin is rotated, but correlation effects will make it inexact when all of the spins are simultaneously rotated. In practice, the correlation effects will give positive and negative contributions that roughly average to zero, making the total-energy change approximately $Nk_B T$ after simultaneously applying $\Delta E_{\text{local}} = k_B T$ to every spin.

Finite-temperature spin perturbations equivalent to $T = 5$ K were applied between energy minimization steps during the hysteresis loop calculations discussed below. The specific algorithm was the following:

- (1) Change applied field,
- (2) Minimize energy, resulting energy = E_1 (using above procedure),
- (3) Set counter = 0,
- (4) Save spin configuration, total energy (E_1),
- (5) Perturb spins ($T = 5$ K),
- (6) Minimize energy, resulting energy = E_2 ,
- (7) If $\Delta E = E_2 - E_1 \geq 0$, then set counter = counter + 1, and restore saved spin configuration and energy,
- (8) If $\Delta E < 0$, then repeat steps 3–9,
- (9) If counter < 2, then repeat steps 4–9.

Note that after each perturbation/relaxation step, the lowest energy state is always selected. This algorithm is most appropriate for low temperatures. If higher temperature properties are of interest, it may be useful to apply a Monte Carlo/Metropolis²⁷ procedure for deciding whether to allow an energy increase. The perturbation procedure can also be used to calculate activation energy distributions corresponding to transitions between metastable spin configurations as discussed below.

III. FERRIMAGNETIC NANOPARTICLES

A. Background

Spin canting in ball-milled NiFe_2O_4 ,^{28,29} chemically precipitated $\gamma\text{-Fe}_2\text{O}_3$,³⁰ and acicular $\gamma\text{-Fe}_2\text{O}_3$ recording media particles^{31,32} has been demonstrated via Mössbauer spectroscopy, as a mechanism for moment reduction. Recent polarized neutron-scattering experiments on ball-milled CoFe_2O_4 particles were consistent with a core of aligned spins surrounded by a disordered shell.³³ Similar conclusions were made from a Mössbauer study of chemically precipitated NiFe_2O_4 particles.³⁴ Recently, we proposed that the canted spins are in a surface layer and that they freeze into a spin-glass-like phase at temperatures below 50 K.^{1,2} Thus, the surface spins have multiple configurations for any orientation of the core magnetization. This model accounts for previously reported anomalous behavior, as well as the remarkable irreversibility and time dependent moment in high fields that we have reported.^{1,2} The model also provides an alternative to macroscopic quantum tunneling (MQT) for interpretation of our magnetization relaxation measurements at low temperatures.³⁵ More recently, evidence for spin-glass-like behavior of surface spins of $\gamma\text{-Fe}_2\text{O}_3$ nanoparticles via quasielastic neutron scattering and ferromagnetic resonance measurements was reported.³⁶

B. NiFe_2O_4 nanoparticles

Fine particle samples were produced by grinding coarse powders (1–2 μm) of high-purity NiFe_2O_4 in kerosene and oleic acid (organic surfactant). The milling was carried out for 1000 h, and the fine-particle component was extracted by centrifugation. The samples were washed of excess surfactant and dried. It was found that approximately one monolayer of oleic acid remained strongly bonded to the surface, and could not be removed by chemical means.²⁹ It was de-

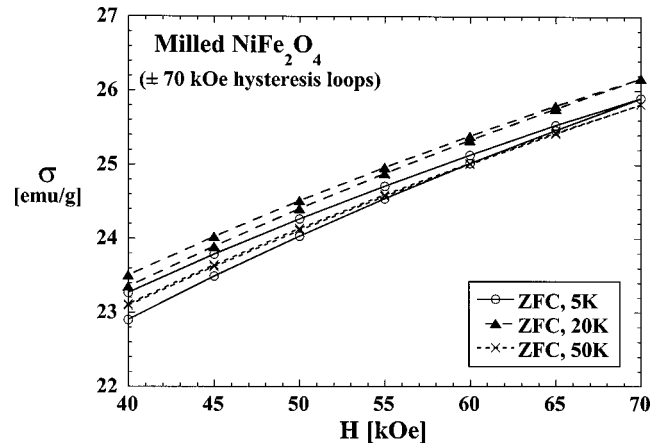


FIG. 1. High-field portion of magnetization hysteresis loops of NiFe_2O_4 nanoparticles measured at 5, 20, and 50 K. Only the positive field portion of a full ± 70 kOe cycle is shown.

termined by TEM studies and x-ray-diffraction line breadths that the average particle size is 65 Å, with a dispersion of about 50%. High-resolution TEM studies on an identically prepared CoFe_2O_4 sample showed that the cubic spinel structure was preserved, and that the particles are for the most part equiaxed single crystals.³⁷

The nanoparticle samples exhibit remarkable high-field irreversibility of the magnetization at temperatures below 50 K. Measurements¹ using a water-cooled Bitter magnet at 4.2 K showed open hysteresis loops, with positive and negative field sweeps separated, up to approximately 160 kOe. This separation implies that some of the magnetic spins have a “switching field” of 160 kOe. The temperature dependence of the high-field magnetization behavior was investigated by a series of measurements on a superconducting quantum interference device (SQUID) magnetometer. Figure 1 shows the high-field portion of loops measured to ± 70 kOe at 5, 20, and 50 K. We note that the high-field differential susceptibility is roughly independent of temperature, which is consistent with the surface spin-canting model, and not consistent with paramagnetism or superparamagnetism which would show a stronger temperature dependence. We also find that the high-field hysteresis decreases at higher temperatures, and is negligible at 50 K.

Low-temperature hysteresis measurements² showed that the coercivity and loop shift decrease rapidly with increasing temperature, with the loop shift vanishing near 50 K. We associate the onset of the loop shift and high-field irreversibility at about 50 K with a “freezing” of disordered surface spins. It is noteworthy that the coercivity has a similar temperature dependence as the loop shift, since it suggests that the coupling with the frozen disordered surface spins makes core spin reversal more difficult.

Magnetization vs time was measured at temperatures down to 0.4 K after application and removal of a 60 kOe field.³⁵ The time dependence of the remanent magnetization was fitted to a logarithmic function, where the viscosity parameter $(1/M_0)dM/d(\ln t)$ is the prefactor of the logarithmic term. The magnetic viscosity vs temperature extrapolated to a nonzero value at zero temperature, and was roughly constant below 2 K.

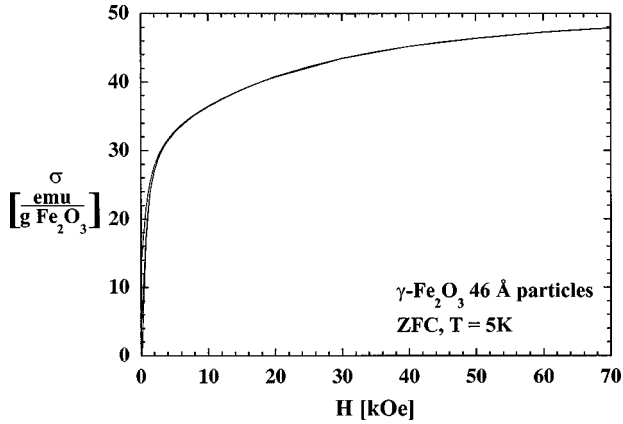


FIG. 2. Hysteresis loop of γ - Fe_2O_3 nanoparticles measured at 5 K (zero-field cooled). Only the first quadrant of a full ± 70 kOe cycle is shown.

C. γ - Fe_2O_3 nanoparticles

Aqueous colloids of γ - Fe_2O_3 (Samples were provided by Dr. Elisabeth Tronc at Universite Pierre et Marie Curie, Paris, France. Sample preparation and characterization by Dr. Tronc and co-workers were reported in Refs. 38 and 39.) were prepared by coprecipitating a $\text{Fe}^{2+} + 2\text{Fe}^{3+}$ mixture with NH_3 , as described in Ref. 38. A solution of the polymer polyvinyl alcohol, PVA, was added, giving homogeneous and rigid films upon drying at room temperature. Characterization was done by chemical analysis, x-ray diffraction, TEM, and Mössbauer spectroscopy to determine the composition, structure and particle size.³⁹ We measured magnetization vs field in zero-field-cooled and field-cooled conditions using a SQUID magnetometer. Figure 2 shows the first quadrant of a full ± 70 kOe hysteresis loop. The loop closes at a relatively low field (~ 4 kOe), indicating that there is no high-field irreversibility such as we found for the NiFe_2O_4 nanoparticles. However, the moment is unsaturated up to the maximum field of 70 kOe, similar to what was found for the NiFe_2O_4 , consistent with surface spin canting. Further, we find a hysteresis loop shift upon field cooling to 5 K in a +70 kOe field, as shown in Fig. 3.

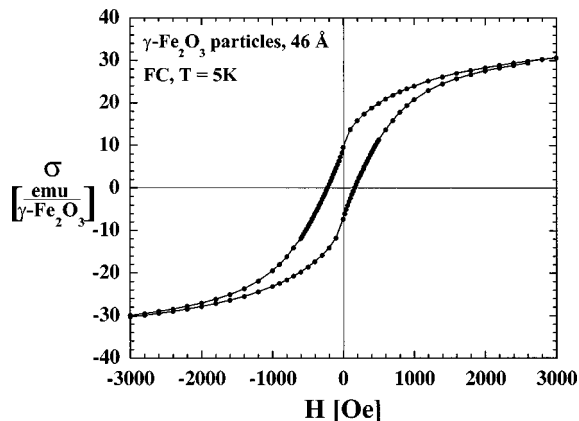


FIG. 3. Low-field portion of a ± 70 kOe hysteresis loop of γ - Fe_2O_3 nanoparticles measured at 5 K. The cooling field was +70 kOe.

D. Discussion of experiment

Sufficiently small magnetic particles are usually single domains, with atomic spins completely aligned by exchange interactions. The rotational barriers due to magnetocrystalline, magnetoelastic, and shape anisotropy can trap such particles in two or more metastable orientations, giving rise to hysteresis. The persistence of hysteresis up to 160 kOe in the NiFe_2O_4 nanoparticles could be interpreted as resulting from anisotropy fields of 160 kOe. However, this is 400 times larger than the bulk magnetocrystalline anisotropy field. Our observation of shifted hysteresis loops suggests that the surface spins are spin-glass-like, having multiple configurations that become frozen below 50 K. Due to the exchange coupling between the surface and core spins, field cooling can select a surface spin configuration which favors the particle being magnetized in the field-cooling direction, hence resulting in a shifted hysteresis loop below 50 K. The field required to force transitions between surface spin configurations can be very large since the exchange fields are approximately 5×10^6 Oe. Therefore, our interpretation is that the open hysteresis loop at high field is the result of irreversible changes between these surface spin configurations rather than reversals of particle magnetization as a whole. Time-dependent magnetization of a fine particle system is usually modeled in terms of thermal activation of particles with two stable magnetization states. Within our surface spin disorder model, time-dependent magnetization may not *only* be due to particles reversing their orientation of magnetization, but also result from thermally activated transitions between surface spin configurations. This has significance in interpreting our measurements of the time decay of remanent magnetization for the NiFe_2O_4 nanoparticles, for which we observed a temperature-independent viscosity parameter from 2.0 K down to 0.4 K. Such a crossover into a temperature-independent regime is predicted for MQT of single-domain particles,⁷ however it also has been shown that a distribution of energy barriers $n(E) \sim 1/E$ gives crossover behavior for thermal activation.⁵ This type of barrier distribution is not consistent with single-domain particles, but it *is* consistent with a spin-glass-like collection of surface spins, as demonstrated below.

Measurements on chemically precipitated γ - Fe_2O_3 nanoparticles show some but not all of the same features as the NiFe_2O_4 nanoparticles. The moment is unsaturated and has a large differential susceptibility at high field. This was noted by Coey in his seminal work on similarly prepared γ - Fe_2O_3 nanoparticles.³⁰ He additionally noted the lack of paramagnetism in the Mössbauer spectrum at low temperature, indicating spin canting rather than a nonmagnetic surface layer. We also find a shifted hysteresis loop upon field cooling this sample, which can be explained on similar grounds as for the NiFe_2O_4 nanoparticles. What is missing is the high-field irreversibility, which we will discuss below in Sec. III F.

E. Modeling: NiFe_2O_4

The exchange constants⁴⁰ are the following (in units of K):

$$J_{AA} = -21.0, \quad J_{AB} = -36.0, \quad J_{AB'} = -28.1$$

$$J_{BB} = -22.0, \quad J_{BB} = +2.0, \quad J_{B'B'} = -8.6 \quad (15)$$

where $A = (\text{Fe}^{3+}, \text{tetrahedral site})$, $B = (\text{Ni}^{2+}, \text{octahedral site})$, $B' = (\text{Fe}^{3+}, \text{octahedral site})$. The small size of the exchange constants relative to the ordering temperature (838 K) of NiFe_2O_4 is due to the large coordination; A sites having 16 neighbors and B sites having 12 neighbors.

Approximately spherical particles were generated by including all sites on a spinel lattice within a spherical volume. In the following discussion, ‘‘surface cations’’ are those with lower than bulk coordination. Surface roughness was created by removing surface cations at random. The fraction of *surface* cations removed in this way we refer to as the surface vacancy density (SVD). Following this procedure we removed any asperities, defined as cations with fewer than two nearest neighbors. As indicated in Sec. II, a fraction of the exchange energy terms between surface cations were removed, breaking the exchange bond between them. The fraction of broken exchange bonds relative to the total number of neighboring pairs of surface cations we refer to as the broken bond density (BBD).

Surface anisotropy. As discussed in Sec. II, we expect large perturbations to the crystal field at surface sites resulting in surface anisotropy. Values of k_S between 1–4 k_B /spin were chosen for the calculations, and are representative of the magnitudes determined by EPR measurements of the anisotropy of dilute Ni^{2+} and Fe^{3+} in various oxide host crystals.^{20,21} We treat this surface anisotropy as uniaxial, with the axis defined by the dipole moment of the neighboring ions. Hence, the easy axis for these ions is approximately radial. It is intuitively clear that if the spins were perfectly aligned (i.e., no surface spin disorder), that the effect of a radially symmetric surface anisotropy would average to zero. This is demonstrated in Fig. 4(a), which shows a calculated hysteresis loop for a 25 Å NiFe_2O_4 particle having no broken exchange bonds (BBD=0) or additional roughness (SVD=0), but with a surface anisotropy of 4 k_B /spin included. For this case, there is no surface spin disorder and we find that the effect of the surface anisotropy indeed averages to zero, hence the coercivity is vanishingly small. In contrast, Fig. 4(b) shows a calculated hysteresis loop for the same particle size with SVD=0.15 and BBD=0.8, plus a surface anisotropy of 4 k_B /spin. We find that when there is surface spin disorder the surface anisotropy results in an enhanced coercivity (1800 Oe in this example), as well as irreversibility up to about 10 kOe.

The effect of the surface anisotropy becomes more pronounced when more roughness is added. For example, Fig. 5 shows a 40 Å NiFe_2O_4 particle with SVD=0.1/0.1/0.1 and BBD=0.8. This threefold surface vacancy density indicates that first 10% of the surface cations are removed as described previously, then the cations are reclassified to determine which cations are on the surface and the procedure is repeated twice. Finally, any asperities are removed as described previously. This iterative procedure promotes a more irregular surface, since the roughness is no longer limited to the outermost monolayer of the initial sphere. The high-field irreversibility is quite pronounced, the loop being open up to approximately 60 kOe. The spin configuration at +50 kOe, during the downward field sweep, is shown in Fig. 6. The nature of the high-field irreversibility can be seen by com-

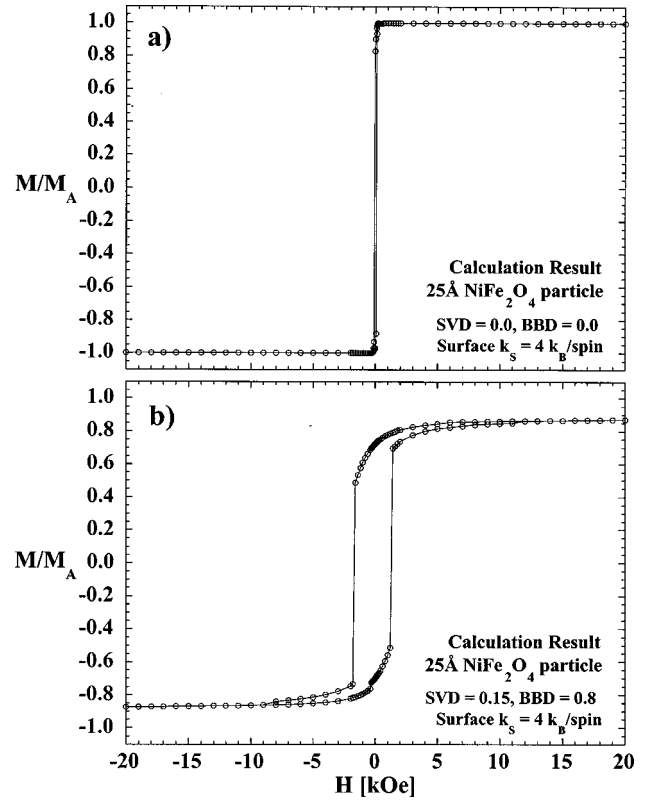


FIG. 4. Calculated hysteresis loops for a 25 Å NiFe_2O_4 particle, with a surface anisotropy of 4 k_B /spin. (a) Particle with no broken bonds or additional roughness, hence no surface spin disorder. (b) Particle with surface vacancy density SVD=0.15, and broken bond density BBD=0.8, hence significant surface spin disorder. The combination of surface anisotropy and surface spin disorder leads to high-field irreversibility.

paring the spin configurations in the upward and downward field sweeps. Figure 7 shows the difference $\hat{S}(H, \text{upsweep})_i - \hat{S}(H, \text{downsweep})_i$ between the two configurations at +50 kOe. This figure is a projection of *all* of the spins in the particle along the $\langle 1\bar{1}0 \rangle$ axis, so in most cases there are

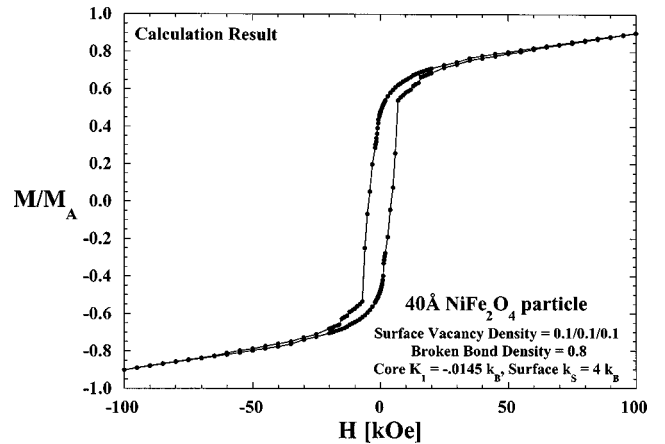


FIG. 5. Calculated hysteresis loop for a 40 Å NiFe_2O_4 particle, with surface vacancy density SVD=0.1/0.1/0.1, and broken bond density BBD=0.8. The three SVD parameters are applied iteratively as described in the text. A surface anisotropy of 4 k_B /spin is included.

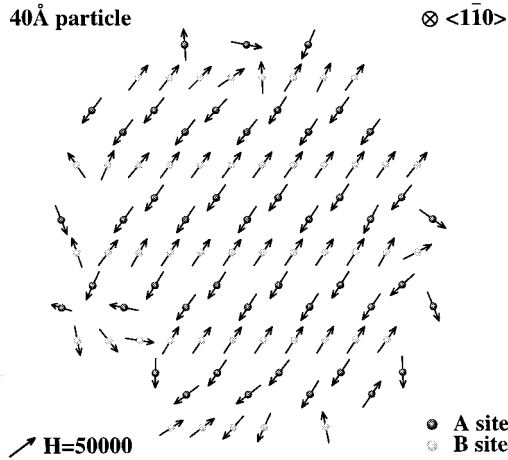


FIG. 6. Calculated spin configuration at $H = +50$ kOe, during the downward field sweep, for a cross section of a 40 Å NiFe_2O_4 particle. Parameters are identical to those used in Fig. 5.

several sites overlaid upon each other. The difference vectors are denoted by arrows whose lengths indicate the magnitude of the difference. Sites at which there is no difference are indicated by a small dot, and the longest arrows correspond to complete reversals of spins. A noteworthy feature of this figure is that there are often neighboring pairs of spins which both flip 180° . This results in a slightly different net moment because the different cations have different moments [$\mu(\text{Fe}^{3+}) \approx 5\mu_B$, $\mu(\text{Ni}^{2+}) \approx 2\mu_B$].

Activation energies. Since we are interested in the time dependence of the moment of such a particle, we developed a method to calculate the activation energies associated with transitions between surface spin states. States are found by perturbing an initial configuration with a random set of rotations, as described in Sec. II. A perturbation energy of 30

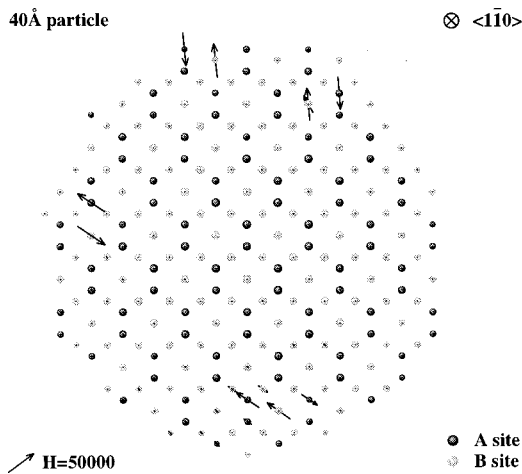


FIG. 7. Difference between calculated spin configurations for a 40 Å NiFe_2O_4 particle at +50 kOe during up-sweep and down-sweep of the field in a hysteresis loop. Sites at which there is no difference are indicated by a dot, and the longest arrows correspond to complete reversals of spins. This is a projection of *all* of the sites in the particle along the $\langle 1\bar{1}0 \rangle$ axis, so in most cases there are several sites overlaid upon each other. Parameters are identical to those used in Figs. 5 and 6.

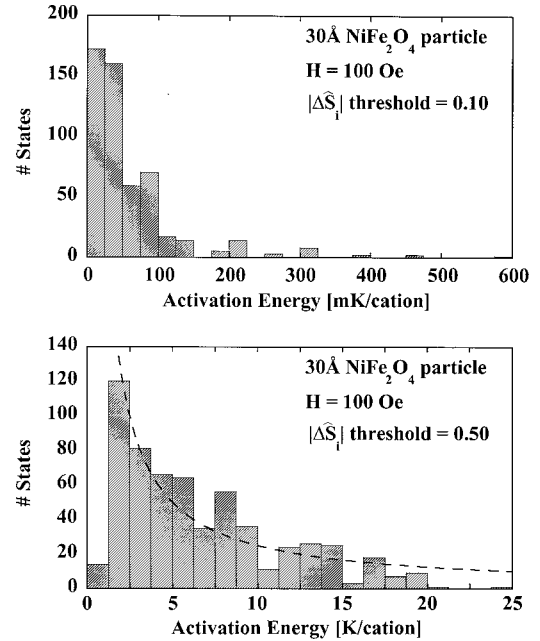


FIG. 8. Calculated activation energy distribution for a 30 Å NiFe_2O_4 particle with surface anisotropy of $4k_B$ /spin, using values of 0.1 and 0.5 for the $|\Delta\hat{S}_i|$ threshold. Note the larger energy units of the bottom histogram (K cation rather than mK/cation).

K/spin was used, and a set of 600 distinct states were recorded, each time checking that the new state differed by $|\Delta\hat{S}_i| > 0.02$ from each of the previously recorded states. Each state was tested for stability by applying a perturbation three times and checking that each time it converged back to the same state, i.e., $|\Delta\hat{S}_i|$ less than a threshold value. The perturbation was made small initially, then made incrementally larger until the state was no longer stable under that perturbation. We define the ‘‘activation energy’’ as the perturbation energy required to make the spins converge to a different state, i.e., $|\Delta\hat{S}_i| > 0.02$.

We find that there is a hierarchy of states in the neighborhood of any starting state. If a state is perturbed by a small energy, it can relax to another state which differs from the original state by a small amount (i.e., $|\Delta\hat{S}_i|$ is small). However, if the state is perturbed by a large energy, it can relax to another state which differs by a large amount (i.e., $|\Delta\hat{S}_i|$ is large). We characterized this hierarchy of states by repeating the activation energy calculation using different values of the threshold for $|\Delta\hat{S}_i|$ in the stability criterion. Results for this calculation on a 30 Å particle with surface anisotropy $k_s = 4k_B$ using $|\Delta\hat{S}_i|$ threshold values of 0.1 and 0.5 are shown in Fig. 8. The dashed curve is a fit to $1/E$, which appears appropriate for a limited energy range (2–20 K). We consider the experimental window, as discussed in Sec. I, corresponding to these energy barriers. Using the value $f_0 = 3 \times 10^9 \text{ s}^{-1}$ obtained for $\gamma\text{-Fe}_2\text{O}_3$ nanoparticles,⁴¹ these barriers correspond to an experimental window of $T = 0.07\text{--}0.7$ K for relaxation measurements where $t \approx 1000$ s. This implies that thermally activated relaxation of this system would be temperature independent at low tem-

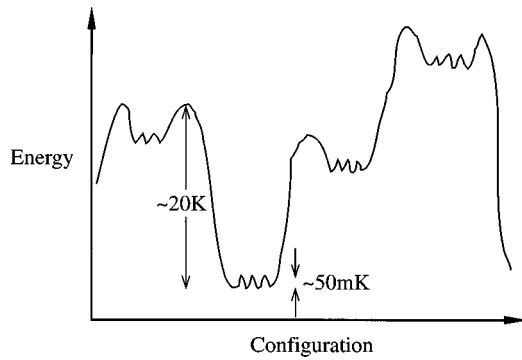


FIG. 9. Pictorial description of the energy landscape for a NiFe_2O_4 nanoparticle with surface anisotropy. Configuration space is indicated on the horizontal axis and energy is indicated on the vertical axis.

peratures, similar to what we found experimentally.³⁵ Calculations of activation energies in the absence of surface anisotropy were reported previously,¹ and were qualitatively similar but quantitatively much smaller (~ 50 mK).

A detailed treatment of the relaxation of such a many-state system is a nontrivial problem. The hierarchical distribution of barriers is similar to ones described for other systems with many degrees of freedom such as spin glasses and folding proteins. One way to pictorially describe the “energy landscape” is shown in Fig. 9, where the $2N$ -dimensional configuration space is indicated schematically in one dimension along the horizontal axis, and the energy is indicated along the vertical axis. In the vicinity of each state, there is a “family” of local equilibria which can be accessed with only a small activation energy (a few mK, in this case). The $|\Delta\hat{S}_i|$ threshold specifies how far away in configuration space the system must be excited before we consider it to be in a different state. Once the $|\Delta\hat{S}_i|$ threshold is large enough to span the family of local equilibria, we begin to probe the higher activation energies in the distribution.

F. Modeling: $\gamma\text{-Fe}_2\text{O}_3$

As shown in Fig. 7, we found that the high-field irreversibility in NiFe_2O_4 was primarily due to pairs of surface spins which reverse together. It would appear that this type of irreversibility would not occur if all of the cations had the same moment. Such is the case for $\gamma\text{-Fe}_2\text{O}_3$, which only contains Fe^{3+} ions, and indeed we do not observe high-field irreversibility in samples of $\gamma\text{-Fe}_2\text{O}_3$ nanoparticles, as shown in Fig. 2. However, detailed modeling of spin configurations of $\gamma\text{-Fe}_2\text{O}_3$ nanoparticles did exhibit similar tendencies for high-field irreversibility for the same values of surface anisotropy and roughness. We used the exchange constants of NiFe_2O_4 which correspond to Fe^{3+} pair interactions:

$$J_{AA} = -21.0, \quad J_{AB'} = -28.1, \quad J_{B'B'} = -8.6 \quad (16)$$

[using the same notation as in Eq. (15)]. Using the Néel model⁴² to estimate the corresponding T_c gives a value of 905 K, which is consistent with experimental estimates of the T_c for $\gamma\text{-Fe}_2\text{O}_3$ in the literature.⁴³ Since the evidence for vacancy ordering is unclear for small particles,⁴³ we assumed a random distribution of octahedral vacancies. Figure 10(a)

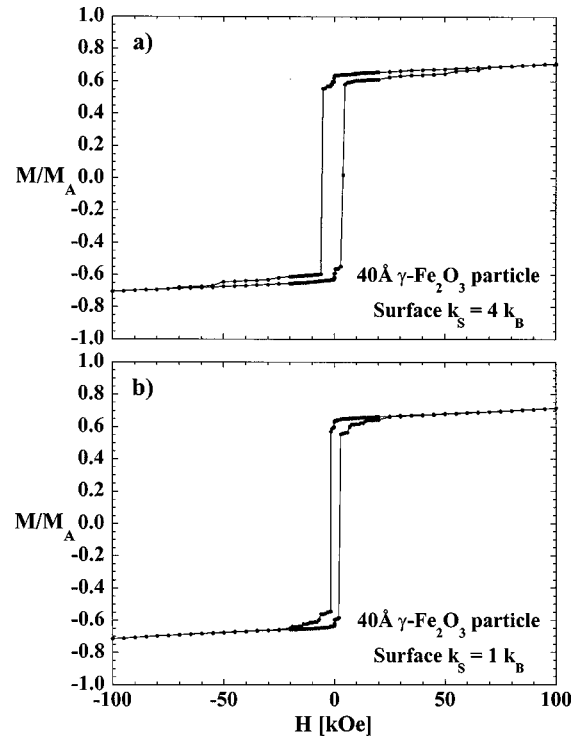


FIG. 10. Calculated hysteresis loops for 40 \AA $\gamma\text{-Fe}_2\text{O}_3$ particles, with surface vacancy density $\text{SVD}=0.1/0.1/0.1$, and broken bond density $\text{BBD}=0.8$. The particle shown in (a) has a surface anisotropy of $4 k_B/\text{spin}$, whereas (b) has a surface anisotropy of $1 k_B/\text{spin}$.

shows a calculated hysteresis loop for a 40 \AA $\gamma\text{-Fe}_2\text{O}_3$ particle having the same roughness and surface anisotropy parameters as those used in Fig. 5. The high-field irreversibility is clearly present, in addition to the reduced moment and lack of saturation due to surface spin disorder. The lack of high-field irreversibility in the experimental data of Fig. 2 suggests that the surface anisotropy may be less for the chemically prepared specimens. We have calculated the hysteresis loop corresponding to a surface anisotropy of $1 k_B/\text{spin}$, rather than $4 k_B/\text{spin}$. This result is shown in Fig. 10(b), where we see that the high-field irreversibility and large coercivity are no longer present. A lower surface anisotropy could result from different ligands bonded surface cations, leading to different crystal-field splittings. Experimental testing of this hypothesis would require further study.

G. Summary

We have observed high-field irreversibility in the moment versus field and moment versus temperature of NiFe_2O_4 nanoparticles. The onset temperature of this irreversibility is near 50 K. Earlier investigations established that there is spin canting in these particles. The appearance of shifted hysteresis loops lead us to propose that the canted spins are on the particle surfaces, and have multiple stable configurations, one of which is selected by field cooling. We additionally suggested that the open hysteresis loops and time-dependent moment are due to transitions between surface spin configurations, rather than magnetization reversals of whole particles. Our numerical model demonstrates the potential for surface spin disorder, arising from reduced coordination and

broken exchange bonds between surface spins. Calculation of the energy barrier distribution between surface spin states is consistent with $n(E) \sim 1/E$ which has been shown to produce a thermally activated temperature-independent viscosity. Thus, a temperature-independent viscosity is not necessarily an indicator of MQT in fine-particle systems where spin disorder is present. A model of surface anisotropy is given, based on consideration of crystal field splitting of surface spin states. The combination of surface spin disorder and surface anisotropy accounts for the observed high-field irreversibility and gives energy barriers of the correct order of magnitude to explain the low-temperature relaxation. For chemically precipitated γ -Fe₂O₃ nanoparticles, we find unsaturated magnetization, consistent with surface spin disorder, but no high-field irreversibility. We suggest that the lack of high-field irreversibility is due to smaller surface anisotropy in these particles as a result of different ligands bonded to surface cations.

IV. ANTIFERROMAGNETIC NANOPARTICLES

A. Background

Néel suggested in 1961 that fine particles of an antiferromagnetic material should exhibit magnetic properties such as superparamagnetism and weak ferromagnetism.⁴⁴ Néel attributed the permanent magnetic moment to an uncompensated number of spins on two sublattices. Indeed, large magnetic moments in antiferromagnetic nanoparticles have been observed in materials such as NiO,^{45–47} however, their origin is not clear. Some investigators attributed these moments to nonstoichiometry, presence of superparamagnetic metallic nickel clusters or Ni³⁺ ions within the NiO lattice.⁴⁸ However, a recent report⁴⁹ has shown that these moments are only slightly changed by mild reduction (to eliminate Ni³⁺) or oxidation (to eliminate Ni metal). Our recent experimental work^{50,3} has shown that NiO nanoparticles also exhibit remarkable hysteresis at low temperatures, having coercivities and loop shifts of up to 10 kOe. This behavior is difficult to understand in terms of the two-sublattice antiferromagnetic ordering which is accepted for bulk NiO. Numerical modeling of spin configurations in these nanoparticles yields eight, six, or four-sublattice configurations, indicating a finite-size effect, in which the reduced coordination of surface spins causes a fundamental change in the magnetic order throughout the particle. The relatively weak coupling between the sublattices allows a variety of reversal paths for the spins upon cycling the applied field, resulting in large coercivities and loop shifts when bulk and surface anisotropies are included.

B. Experiment

Following the method used by Richardson,⁴⁵ nickel hydroxide Ni(OH)₂ precursor was chemically precipitated by mixing a nickel nitrate Ni(NO₃)₂·6H₂O aqueous solution and a sodium hydroxide NaOH aqueous solution. NiO nanoparticles of various sizes were prepared by calcining portions of the dried gel for 3 h at various temperatures.⁵⁰ X-ray-diffraction patterns indicate single phase fcc NiO. The particle size was estimated from both x-ray-diffraction line broadening using a modified Debye-Scherrer method,⁵¹ and

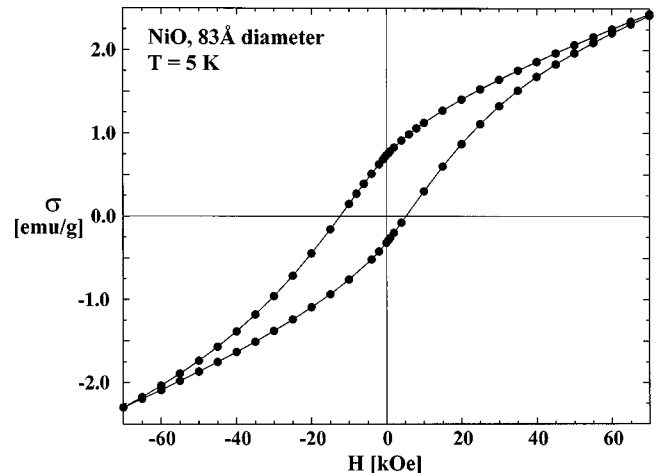


FIG. 11. Hysteresis loop at 5 K of 83 Å NiO particles field cooled from 340 K in +20 kOe.

Brunauer-Emmett-Teller surface area measurements assuming spherical particles. TEM measurements are consistent with these size determinations, and suggest the possibility of platelet-shaped particles.

Large coercivities and shifted hysteresis loops were observed for all samples after field cooling. Measurements at 5 K on a sample having an average diameter of the 83 Å, field cooled in +20 kOe from 340 to 5 K are shown in Fig. 11. For this sample the coercivity is 8.8 kOe, and the loop shift is 3.7 kOe. Very large coercivities and exchange fields (>10 kOe) are also obtained for the intermediate sized particles with $220 \text{ Å} \leq d \leq 315 \text{ Å}$.³

C. Modeling

The hysteresis of a collection of two-sublattice antiferromagnetic nanoparticles, having net moments due to uncompensated spins, can be described in terms of a Stoner-Wohlfarth type model,⁵² in which the spin axis has two or more metastable orientations, which depend on the magnetic anisotropy and the applied field. Within this model, *major* hysteresis loops are symmetric since the magnetocrystalline anisotropy has inversion symmetry. If, however, the field is not sufficient to reverse the particle moment (i.e., minor hysteresis loop), one could obtain a shifted loop with no hysteresis. Therefore, a simultaneous loop shift and coercivity can only be described in terms of this model if one attributes it to a broad distribution of reversal fields, both greater and less than the maximum applied field. In order to better understand the magnetic behavior of antiferromagnetic nanoparticles, we have employed calculations of equilibrium spin configurations as described in Sec. II. The anisotropy of bulk NiO was investigated by Hutchings and Samuelsen⁵³ who used an orthorhombic form for the anisotropy:

$$E_A = D_1 S_z^2 + D_2 S_y^2, \quad (17)$$

where x is the easy axis $\langle 11\bar{2} \rangle$ and z is the hard axis $\langle 111 \rangle$. The structure of NiO is actually rhombohedral so for the calculations we used instead a sixfold symmetric form, consistent with torque measurements.⁵⁴ The anisotropy used in our calculations was

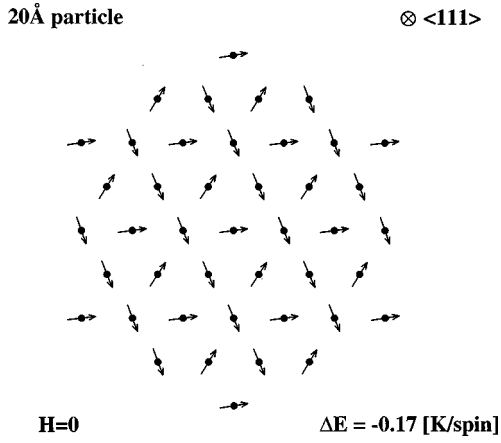


FIG. 12. Equilibrium spin configuration for a 20 Å NiO particle. The (111) cross section is shown, which is ferromagnetically aligned in bulk NiO. Instead, we find six sublattices, instead of the usual two sublattices. The energy difference between this equilibrium state and the two sublattice state is -0.17 K/spin.

$$E_A = D_1 \hat{S}_z^2 - (D_2/18) \cos 6\phi_i \sin^6 \theta_i, \quad (18)$$

where θ_i and ϕ_i are the conventional spherical coordinates corresponding the direction of the ionic spin \hat{S}_i with ϕ_i referenced to the $\langle 11\bar{2} \rangle$ direction. The factor of 18 results from matching the leading terms in a small- ϕ_i expansion of our expression to that of Eq. (17). Following the notation of Ref. 53, the exchange and anisotropy parameters used are the following (in units of K):

$$J_1^+ = 15.7, \quad J_1^- = 16.1, \quad J_2 = -221, \quad (19)$$

$$D_1 = 1.13, \quad D_2 = 0.06,$$

where J_1^- is the exchange integral between spins in the same (111) plane (normally ferromagnetically aligned) and J_1^+ is the exchange integral between spins in adjacent (111) planes (normally antiferromagnetically aligned).

Origin of multisublattice states. Before treating the problem in full detail, it is instructive to consider the case where we neglect the small difference between J_1^+ and J_1^- , associated with the rhombohedral contraction occurring below the Néel point, and also neglect the in-plane anisotropy. The resulting equilibrium spin configurations for particles of 20 and 31 Å are shown in Figs. 12 and 13. These particles are approximately spherical, having no surface roughness or broken exchange bonds. The illustrated (111) cross sections are ferromagnetically aligned in bulk NiO, but instead we find a number of different spin directions. Specifically, we find six sublattices and four sublattices for the 20 and 31 Å particles, respectively, instead of the usual two sublattices. We also indicate the energy difference between the equilibrium state and the two sublattice state as ΔE , which equals -0.17 and -0.25 K/spin for these two cases. In other words, due to the lower coordination at the surface, these multisublattice states have *lower* energies than the two-sublattice state. Based on these four- and six-sublattice configurations, we compute the total exchange energy for a bulk crystal as follows:

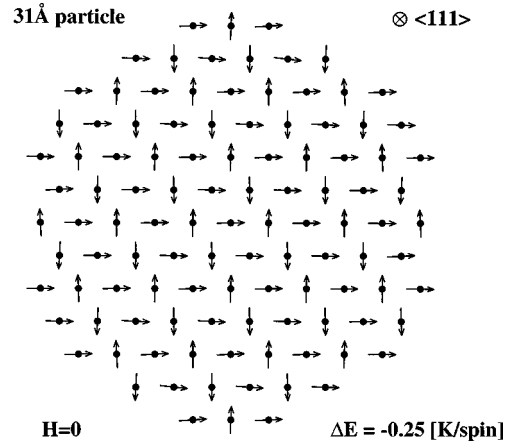


FIG. 13. Equilibrium spin configuration for a 31 Å NiO particle. The (111) cross section is shown, which is ferromagnetically aligned in bulk NiO. Instead, we find four sublattices, instead of the usual two sublattices. The energy difference between this equilibrium state and the two sublattice state is -0.25 K/spin.

No. sublattices	Bulk exchange energy	
2	$6J_2 + 6(J_1^+ - J_1^-)$	$= -1329.1$ K/spin
4	$6J_2$	$= -1326.0$ K/spin
6	$6J_2 + \frac{3}{2}(J_1^+ - J_1^-)$	$= -1326.8$ K/spin

Hence, the only exchange term that makes the two-sublattice state more stable in bulk NiO is proportional to the small $(J_1^+ - J_1^-)$ splitting. We find that the energetic preference for multisublattice states becomes greater when surface roughness and broken exchange bonds are included. Hence, even when the $(J_1^+ - J_1^-)$ splitting is included in the calculations, as described in the next section, the multisublattice states are ground states for smaller particles. This is the essence of the finite-size effect.

Full model calculations. Since J_1^+ and J_1^- are defined based on a two-sublattice spin configuration, it is not immediately obvious how to include the $(J_1^+ - J_1^-)$ in the calculations. We must therefore develop a way of defining how the splitting is to be applied to an arbitrary spin configuration, which handles the two-sublattice configuration as a limiting case. The splitting is associated with the rhombohedral contraction occurring below the Néel temperature, and is believed to be due to the asymmetry in nearest-neighbor atomic spacing depending on whether the neighbor is in the contraction plane. The theory of exchange striction^{55,56} predicts it to vary as

$$J_1^+ - J_1^- = 2j\bar{S}^2, \quad (20)$$

where \bar{S} is the average spin and $j = -0.26$ K.⁵³ \bar{S} can be described as an order parameter for the two-sublattice state. Since we find substantial deviations from the two-sublattice state, we calculate \bar{S} after each step of the relaxation procedure and rescale J_1 according to Eq. (20). We compute \bar{S} for any given spin configuration as

$$\bar{S} = \max_{j=1,2,3,4} \left| \frac{1}{N} \sum_{i=1}^N (-1)^{k_{ij}} \mathbf{S}_i \right|, \quad (21)$$

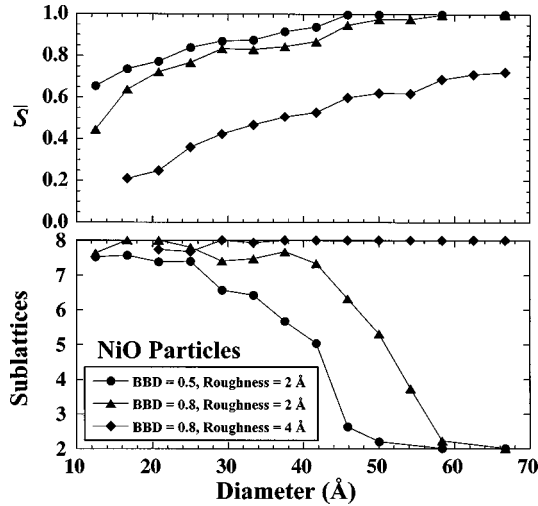


FIG. 14. Calculated average order parameter \bar{S} and average number of sublattices for 30 different NiO particles in zero applied field as a function of diameter. The surface broken bond density (BBD), and rms roughness amplitude are indicated in the legend.

where N is the number of spins, and k_{ij} is defined as

$$\begin{aligned} k_{i1} &= \mathbf{P}_i \cdot (1, 1, 1)/a, \\ k_{i2} &= \mathbf{P}_i \cdot (1, 1, -1)/a, \\ k_{i3} &= \mathbf{P}_i \cdot (1, -1, 1)/a, \\ k_{i4} &= \mathbf{P}_i \cdot (-1, 1, 1)/a, \end{aligned} \quad (22)$$

where \mathbf{P}_i is the position of the i th spin and a is the cubic lattice parameter. We essentially calculate the order parameter for each possible (111)-type ordering plane, and take the largest value. The magnitude of the uniaxial surface anisotropy was chosen to be 2 K, which is a reasonable value based on EPR determinations of the magnetocrystalline anisotropy of Ni^{2+} ions in bulk oxide crystals with sites of low symmetry.²⁰

Calculations on spherical particles of different diameters were performed in order to determine the onset of the multisublattice spin state. Figure 14 shows the order parameter \bar{S} and the average number of sublattices for 30 different particles in zero applied field as a function of particle diameter. Two curves are plotted for relatively smooth particles with different values of the broken bond density (BBD), and a third curve is plotted for a rougher particle. Roughness is created by removing surface cations at random and taking off any asperities afterward, as described in Sec. II. The results indicate that the order parameter approaches unity as the particle size increases, while the average number of sublattices is close to 8 for smaller sizes and approaches 2 as the size increases. The size threshold for this behavior is strongly dependent on parameters of the surface.

Hysteresis loops were calculated for both spherical and platelet shaped particles and in both cases we found large coercivities and loop shifts. A simulated field-cooling procedure was performed, in which perturbations of 400 K/spin were applied and the spin configuration was allowed to relax in the presence of a 100 kOe field. The perturbation was

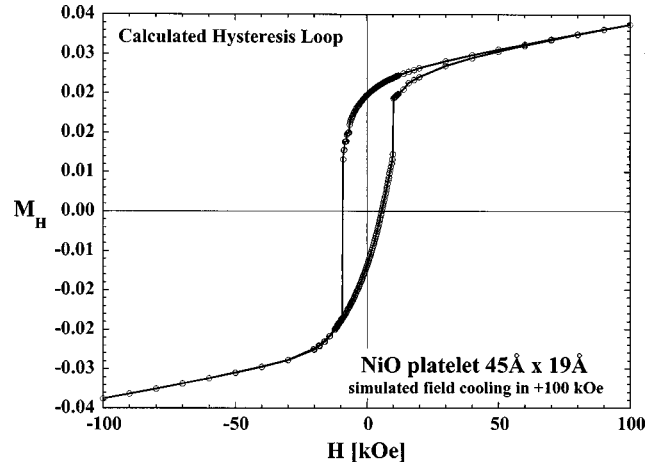


FIG. 15. Calculated field-cooled hysteresis loop for a 45 Å diameter, 19 Å thick NiO platelet. Field is applied in the plane of the platelet, which has $\langle 111 \rangle$ orientation.

applied several times, followed by relaxation of the spin configuration each time, to find the lowest energy state. An example of such a calculation is shown in Fig. 15, for a 45 Å diameter, 19 Å thick platelet, with the field applied in the plane of the platelet, which has $\langle 111 \rangle$ orientation. The broken bond density in this case was 0.5. The calculated curve exhibits a large coercivity and loop shift as was found experimentally (e.g., Fig. 11). As discussed in Ref. 3, the spin configurations in the positive and negative remanent states are complex multisublattice states and are qualitatively different, not simply 180° rotations from each other. The inter-sublattice angles are not fixed, but change substantially upon cycling the field, giving rise to a variety of reversal paths for the spins. We find that surface anisotropy and multisublattice states are key ingredients to produce simultaneous coercivities and shifted loops.

Based on our calculated spin configurations, we find that the stability of the two-sublattice state (versus multisublattice states) in bulk NiO is directly related to the $(J_1^+ - J_1^-)$ splitting. Since the rhombohedral contraction is known to diminish with increasing temperature,⁵⁶ multisublattice states should become more prevalent at higher temperatures. We suggest that considerations of multisublattice ordering may be useful in describing critical behavior, even in bulk NiO.

In summary, we have observed large moments in NiO nanoparticles, as well as large coercivities and loop shifts at low temperatures. These observations are consistent with multisublattice spin configurations which follow directly from bulk exchange parameters and considerations of low coordination at surface sites. Specifically, we find that the stability of the two-sublattice state over multisublattice states in bulk NiO is directly related to the small exchange term $(J_1^+ - J_1^-)$, and that the low coordination at surface sites tends to make multisublattice states more stable. This competition between bulk and surface energies results in the finite-size effect. We show that this finite-size effect can have a profound effect on low-temperature hysteresis properties, giving rise to simultaneous coercivity and loop shift when surface and bulk anisotropies are included. We suggest that multisublattice states become more important at high temperatures, even in bulk materials.

ACKNOWLEDGMENTS

High-field magnetization data were taken by Ed McNiff at the Francis Bitter National Magnet Laboratory (FBNML). Low-temperature relaxation measurements were performed with the assistance of Christopher Seaman at UCSD. Thanks to Elisabeth Tronc for providing the γ -Fe₂O₃ nanoparticle

samples. Salah Makhlof performed most of the experimental work on NiO nanoparticles. TEM investigation of NiO nanoparticles was performed by Gregory Fischer and Lea Rudee at UCSD. Thanks to Simon Foner at FBNML for many valuable discussions. This work was supported by the MRSEC Program of the NSF under Award No. DMR-9400439.

*Present address: Naval Research Laboratory, Code 6342, 4555 Overlook Ave. SW, Washington, DC 20375.

¹R. H. Kodama, A. E. Berkowitz, E. J. McNiff, Jr., and S. Foner, *Phys. Rev. Lett.* **77**, 394 (1996).

²R. H. Kodama, A. E. Berkowitz, E. J. McNiff, Jr., and S. Foner, *J. Appl. Phys.* **81**, 5552 (1997).

³R. H. Kodama, Salah A. Makhlof, and A. E. Berkowitz, *Phys. Rev. Lett.* **79**, 1393 (1997).

⁴R. Street and J. C. Woolley, *Proc. Phys. Soc. London, Sect. A* **62**, 662 (1949).

⁵B. Barbara, C. Paulsen, L. C. Sampaio, M. Uehara, F. Fruchard, J. L. Tholence, and A. Marchand, *Magnetic Properties of Fine Particles*, edited by J. L. Dormann and D. Fiorani (Elsevier Science, Amsterdam, 1992), p. 235.

⁶C. P. Bean and J. D. Livingston, *J. Appl. Phys.* **30**, 120S (1959).

⁷E. M. Chudnovsky and L. Gunther, *Phys. Rev. Lett.* **60**, 661 (1988).

⁸A. Garg and G.-H. Kim, *Phys. Rev. Lett.* **63**, 2512 (1989).

⁹P. C. E. Stamp, E. M. Chudnovsky, and B. Barbara, *Int. J. Mod. Phys. B* **6**, 1355 (1992).

¹⁰W. F. Brown, *Micromagnetics* (Interscience, New York, 1963).

¹¹J.-G. Zhu and H. N. Bertram, *IEEE Trans. Magn.* **24**, 2706 (1988).

¹²D. R. Fredkin and T. R. Koehler, *IEEE Trans. Magn.* **25**, 3473 (1989).

¹³M. E. Schabes and H. N. Bertram, *J. Appl. Phys.* **64**, 5832 (1988).

¹⁴M. Labruno and J. Miltat, *IEEE Trans. Magn.* **26**, 1521 (1990).

¹⁵K. Kosavitsutte and N. Hayashi, *Jpn. J. Appl. Phys., Part 1* **34**, 5599 (1995).

¹⁶N. C. Koon, *J. Appl. Phys.* **79**, 5841 (1996).

¹⁷W. M. Saslow and N. C. Koon, *Phys. Rev. B* **49**, 3386 (1994).

¹⁸D. P. Pappas, A. P. Popov, A. N. Anisimov, B. V. Reddy, and S. N. Khanna, *Phys. Rev. Lett.* **76**, 4332 (1996).

¹⁹L. Néel, *J. Phys. Radium* **15**, 225 (1954).

²⁰A. K. Petrosyan and A. A. Mirzakhanyan, *Phys. Status Solidi B* **133**, 315 (1986).

²¹E. S. Kirkpatrick, K. A. Müller, and R. S. Rubins, *Phys. Rev.* **135**, A86 (1964).

²²W. Low, *Paramagnetic Resonance in Solids* (Academic, New York, 1960), p. 33.

²³W. F. Brown, *J. Appl. Phys.* **33S**, 1308 (1962).

²⁴G. F. Hughes, *J. Appl. Phys.* **54**, 5306 (1983).

²⁵The second derivatives for cubic anisotropy can be written in a form where the cubic symmetry is more apparent (the form shown in the main text is slightly more compact for computational efficiency):

$$\frac{\partial^2 E}{\partial \alpha_j \partial \alpha_i} = \begin{cases} +g_i \mu_B S_i (\hat{S}_{0i} \cdot \mathbf{H}_{\text{eff}}) - 2k_1 [1 - \hat{e}_{aix} \hat{S}_{0ix}^2 - \hat{e}_{aiy} \hat{S}_{0iy}^2 - \hat{e}_{aiz} \hat{S}_{0iz}^2 + 4(\hat{e}_{aix} \hat{S}_{0ix} \hat{e}_{aiy} \hat{S}_{0iy} + \hat{e}_{aiy} \hat{S}_{0iy} + \hat{e}_{aiz} \hat{S}_{0iz} + \hat{e}_{aiz} \hat{S}_{0iz} \hat{e}_{aix} \hat{S}_{0ix})], & i=j \\ -2J_{ij} S_i S_j \hat{e}_{ai} \cdot \hat{e}_{aj} - g_i g_j \mu_B^2 S_i S_j \\ \times \left[\frac{3\hat{r}_{ji}(\hat{r}_{ji} \cdot \hat{e}_{aj}) - \hat{e}_{aj}}{|\mathbf{r}_{ji}|^3} \right] \cdot \hat{e}_{ai}, & i \neq j. \end{cases}$$

²⁶H. Goldstein, *Classical Mechanics* (Addison-Wesley, Reading, MA, 1980), p. 165.

²⁷N. Metropolis, A. Rosenbluth, M. Rosenbluth, A. Teller, and E. Teller, *J. Chem. Phys.* **21**, 1087 (1953).

²⁸A. E. Berkowitz, J. A. Lahut, I. S. Jacobs, L. M. Levinson, and D. W. Forester, *Phys. Rev. Lett.* **34**, 594 (1975).

²⁹A. E. Berkowitz, J. A. Lahut, and C. E. VanBuren, *IEEE Trans. Magn.* **MAG-16**, 184 (1980).

³⁰J. M. D. Coey, *Phys. Rev. Lett.* **27**, 1140 (1971).

³¹A. E. Berkowitz, F. T. Parker, F. E. Spada, and D. Margulies, in *Studies of Magnetic Properties of Fine Particles*, edited by J. L. Dormann and D. Fiorani (Elsevier Science, Amsterdam, 1992), p. 309.

³²See A. H. Morrish, in *Studies of Magnetic Properties of Fine Particles* (Ref. 31), p. 181.

³³D. Lin, A. C. Nunes, C. F. Majkrzak, and A. E. Berkowitz, *J. Magn. Magn. Mater.* **145**, 343 (1995).

³⁴A. H. Morrish and K. Haneda, *J. Appl. Phys.* **52**, 2496 (1981).

³⁵R. H. Kodama, A. E. Berkowitz, C. L. Seaman, and M. B. Maple, *J. Appl. Phys.* **75**, 5639 (1994).

³⁶F. Gazeau, E. Dubois, M. Hennion, R. Perzynski, and Yu. Raikher, *Europhys. Lett.* **40**, 575 (1997).

³⁷A. C. Nunes, E. L. Hall, and A. E. Berkowitz, *J. Appl. Phys.* **63**, 5181 (1988).

³⁸J. P. Jolivet, R. Massart, and J.-M. Fruchart, *Nouv. J. Chim.* **7**, 325 (1983).

³⁹E. Tronc and J. P. Jolivet, in *Magnetic Properties of Fine Particles*, edited by J. L. Dormann and D. Fiorani (Elsevier Science, Amsterdam, 1992), p. 199.

⁴⁰A. A. Sidorov, V. P. Suetin, and A. I. Gusev, *Inorg. Mater.* **24**, 1759 (1988); A. A. Sidorov, V. P. Suetin, and V. G. Pokanzan'ev, in *IAdernyi rezonans v tverdogaznykh soedineniakh d-metallov*, edited by V. A. Gubanov (Inst. of Chem., Acad. of Sci., USSR, Sverdlovsk, 1984), pp. 21–31.

⁴¹T. Jonsson, J. Mattsson, P. Nordblad, and P. Svedlindh, *J. Magn. Magn. Mater.* **168**, 269 (1997).

⁴²L. Néel, *Ann. Phys. (Paris)* **3**, 137 (1948).

⁴³A. H. Morrish, in *Crystals: Growth, Properties and Applications*, edited by H. C. Freyhardt (Springer-Verlag, Berlin, 1980), Vol. 2, p. 173.

⁴⁴L. Néel, in *Low Temperature Physics*, edited by C. Dewitt, B.

- Dreyfus, and P. D. de Gennes (Gordon and Beach, New York, 1962), p. 413.
- ⁴⁵J. T. Richardson and W. O. Milligan, *Phys. Rev.* **102**, 1289 (1956).
- ⁴⁶J. Cohen, K. M. Creer, R. Pauthenet, and K. Srivastava, *J. Phys. Soc. Jpn.* **17**, Suppl. B-I, 685 (1962).
- ⁴⁷W. J. Schuele and V. D. Deetscreek, *J. Appl. Phys.* **33**, 1136 (1962).
- ⁴⁸I. S. Jacobs and C. P. Bean, in *Magnetism*, edited by G. T. Rado and H. Suhl (Academic, New York, 1963), Vol. III, p.294.
- ⁴⁹J. T. Richardson, D. I. Yiagas, B. Turk, K. Forster, and M. V. Twigg, *J. Appl. Phys.* **70**, 6977 (1991).
- ⁵⁰Salah A. Makhlouf, F. T. Parker, F. E. Spada, and A. E. Berkowitz, *J. Appl. Phys.* **81**, 5561 (1997).
- ⁵¹G. K. Williamson and W. H. Hall, *Acta Metall.* **1**, 22 (1953).
- ⁵²E. C. Stoner and E. P. Wohlfarth, *Philos. Trans. R. Soc. London, Ser. A* **240**, 599 (1948).
- ⁵³M. T. Hutchings and E. J. Samuelsen, *Phys. Rev. B* **6**, 3447 (1972).
- ⁵⁴K. Kurosawa, M. Miura, and S. Saito, *J. Phys. C* **13**, 1521 (1980).
- ⁵⁵M. E. Lines and E. D. Jones, *Phys. Rev.* **139**, A1313 (1965).
- ⁵⁶L. C. Bartel and B. Morosin, *Phys. Rev. B* **3**, 1039 (1971).